# Calculation of the Propulsive Efficiency for Airships with Stern Thruster *

Thorsten Lutz, Peter Funk, Andreas Jakobi and Siegfried Wagner

*Institute for Aerodynamics and Gas Dynamics*
*University of Stuttgart, Pfaffenwaldring 21*
*D-70550 Stuttgart, Germany*

*Tel.: +49 711 685 3409 Fax: +49 711 685 3438*
*e-mail: {lutz, funk, jakobi, wagner}@iag.uni-stuttgart.de*

**Abstract** A method for the aerodynamic analysis of bodies of revolution with a stern propeller was developed. The viscous flow about the displacement body is determined by a panel method in combination with an integral boundary-layer procedure. Special emphasis is laid on the iterative viscous/inviscid coupling. For this purpose the transpiration technique is applied along with an under-relaxation scheme. The relaxation factor is determined from a local stability analysis of the coupled governing equations. A vortex sheet model is used to calculate the time-averaged influence of the propeller with a fully-relaxed slipstream. Both modules are coupled taking viscous interaction effects into account. The complete tool was applied to analyse airship hulls with stern-mounted thrusters and finally to predict the increased efficiency of wake propellers.

## Nomenclature

| | |
|---|---|
| $a$ | exponent of the power-law profiles |
| $A$ | amplitude |
| $c$ | chord length |
| $c_d$ | drag coefficient |
| $c_D$ | dissipation coefficient |
| $c_f$ | skin-friction coefficient |
| $c_p$ | pressure coefficient |
| $c_P$ | power coefficient of the propeller |
| $c_T$ | thrust coefficient of the propeller |
| $d$ | distance between body stern and propeller disc area |
| $D$ | propeller diameter, drag |
| $D_{\text{Propeller}}$ | propeller-induced hull drag |
| $H_{12} = \frac{\delta_1}{\delta_2}$ | boundary-layer shape factor |
| $H_{32} = \frac{\delta_3}{\delta_2}$ | boundary-layer shape factor |
| $L$ | body length |
| $n$ | wall normal distance, amplification factor of the TS-waves, propeller rotational speed [rps] |
| $P$ | power |
| $r$ | distance |
| $Re_L$ | Reynolds number (reference length $L$) |
| $R$ | body radius, propeller radius |
| $s$ | arc length |
| $S$ | surface area |
| $T$ | propeller thrust |
| $Tu$ | turbulence factor |
| $u$ | local velocity inside the boundary layer |
| $u$, $\sigma$ | error functions |
| $U_e$ | velocity at the boundary-layer edge |
| $U_\infty$ | axial onset flow velocity |
| $\vec{v}$ | velocity vector |
| $v_n$ | transpiration velocity |
| $x, y, z$ | cartesian coordinates |
| $x, r, \theta$ | cylindrical coordinates |

*Presented at the 14th AIAA Lighter-Than-Air Systems Technical Committee Convention and Exhibition, July 15-19, 2001, Akron, Ohio, USA

| | |
|---|---|
| $\alpha$ | angle of attack |
| $\beta$ | propeller twist angle at $\frac{r}{R} = 0.75$ |
| $\delta$ | boundary-layer thickness |
| $\delta_1$ | displacement thickness (axisymmetric definition) |
| $\delta_2$ | momentum thickness (axisymmetric definition) |
| $\delta_3$ | energy thickness (axisymmetric definition) |
| $\overline{\delta}_1$, $\overline{\delta}_2$, $\overline{\delta}_3$ | integral boundary-layer parameters (plane definition) |
| $\eta$ | propeller efficiency |
| $\eta_e$ | propulsive efficiency |
| $\Phi$ | velocity potential |
| $\lambda$ | propeller advance ratio, wave length |
| $\mu$ | relaxation factor, doublet strength |
| $\nu$ | wave number |
| $\rho$ | density |
| $\sigma$ | source singularity strength |
| $\Sigma$ | dimensionless transpiration velocity |

### Subscripts

| | |
|---|---|
| *crit.* | critical value |
| *e* | boundary-layer edge |
| *max* | maximum value |
| *opt* | optimum value |
| *sep* | separation location |
| *tra* | transition location |
| $\infty$ | undisturbed freestream condition |

### Superscripts

| | |
|---|---|
| $(n)$ | iteration step |
| $\sim$ | converged value |

# 1 Introduction

### Fundamental Aerodynamic Effects of Stern-Mounted Propellers

It is well known that an adequately designed stern propeller is more efficient than a propeller with conventional installation. The reason is that the stern-thruster is operating in the viscous wake of the airship hull, i.e. in a flow domain with reduced axial velocity. As discussed in Refs. [7], [10] this lowers the power which is required to obtain a certain thrust. As a consequence, the resulting propeller efficiency $\eta$ (based on $U_\infty$!) is significantly increased and may be well above 100%.

On the other hand, the suction effect of the propeller slipstream accelerates the flow in the tail region of the airship hull which yields an increase of the pressure drag. For obvious reasons, the propeller-induced hull drag as well as the efficiency $\eta$ of the stern-thruster is higher for hull shapes with a blunt tail.

Detailed investigations on aerodynamic effects of airships with stern-propulsion are hardly reported. An exception represent the wind-tunnel tests performed by McLemore [10]. Because of its importance, the main results of these studies shall be summarized. McLemore examined a 1 : 20 scale model ($L \gtrapprox 6m$) of a complete airship configuration with two different stern-mounted propellers which were designed specifically for the flow conditions occuring in the hull wake.

First of all, McLemore measured the thrust coefficient $c_T$, the power coefficient $c_P$ and the efficiency $\eta$ in dependency of the advance ratio $\lambda$. According to the usual definitions these propeller characteristics are given as:

$$c_T = \frac{T}{\frac{\rho}{2} U_\infty^2 \, \pi \, R^2} \tag{1}$$

$$c_P = \frac{P}{\frac{\rho}{2} U_\infty^3 \, \pi \, R^2} \tag{2}$$

$$\eta = \frac{T \, U_\infty}{P} = \frac{c_T}{c_P} \tag{3}$$

$$\lambda = \frac{U_\infty}{n \cdot D} \tag{4}$$

In his experiments, the larger propeller turned out to be very efficient and shows a maximum efficiency of $\eta \approx 140\%$. McLemore pointed out that values of $\eta$ above 100% only result because according to Eq. (3) the efficiency is defined by the thrust-to-power ratio multiplied by the undisturbed freestream velocity $U_\infty$. Actually, the propeller operates in the viscous hull wake where the local velocities are well below $U_\infty$. If the efficiency would be defined based on the local onset flow velocity, the resulting value of $\eta$ would, of course, be lower than 100% also for a stern thruster.

In a second test the characteristics were measured when the propeller produced enough thrust to propel the airship, i.e. for the condition that the thrust is equal to the total airship drag including propeller-induced drag. The maximum efficiency decreased to $\eta \approx 122\%$ which indicates that the design point of the propeller does not exactly match the steady-state flight conditions.

In a last evaluation the *propulsive* efficiency $\eta_e$ was determined which is defined as:

$$\eta_e = \frac{(T - D_{\text{Propeller}}) \cdot U_\infty}{P} \tag{5}$$

This definition accounts for the fact that due to the propeller-hull interference the thrust required to propel the airship is increased by the propeller-induced hull drag $D_{\text{Propeller}}$. This is a more realistic measure to rate the total effectiveness of the propulsive system[1]. For steady-state flight conditions the measured propulsive efficiency was about 103% compared to a value of only 59% resulting for a fin-mounted propeller.

### Previous Investigations and Overview

In the frame of previous investigations [7] a vortex-sheet model to determine the time-averaged velocity-field induced by a propeller with fully-relaxed slipstream was developed. This propeller module was coupled to a panel/boundary-layer method for the analysis of the viscous hull flow. The coupled method enables the correct prediction of the hull drag including propeller effects. However, with the implementation [7], the propeller efficiency was underpredicted since only the *inviscid* onset-flow velocity-field was considered in the evaluation of the propeller characteristics.

In order to allow a correct prediction of the required power and the propeller efficiency the *viscous* velocity profile in the propeller disc area has to be considered. To obtain a realistic boundary-layer profile at the stern of the airship, first of all, a reliable viscous/inviscid coupling of the integral boundary-layer procedure and the panel method is needed. Therefore, the first extention of the model dealt with the implementation of an improved iterative coupling scheme using the transpiration technique. To stabilize the iteration process an under-relaxation technique is necessary. The approach chosen to determine adequate relaxation factors is based on a linearized local stability analysis of the coupled governing equations.

In the subsequent chapter the fundamentals of the panel method and the propeller module are summarized, followed by a more detailed discussion of the boundary-layer procedure and especially of the coupling scheme developed. Sec. 4 is devoted to the application of the enhanced method. First, validation examples with respect to the new viscous/inviscid coupling will be given. Thereafter, the method is applied to calculate the characteristics of a propeller operating in the viscous wake of an airship hull. Comparisons to the experiments of McLemore will be presented.

[1] Another appropriate approach would be to just consider the power (coefficient) needed to propel the airship at a certain speed, regardless of the thrust required.

# 2 Calculation of the Inviscid Outer-Flow Field

In general, the viscous flowfield about a configuration can be calculated by numerically solving the (Reynolds-averaged) Navier-Stokes-equations, which is rather time consuming with respect to mesh-generation and computational effort. This is especially true for a configuration with rotating propeller because this requires an unsteady analysis. If the Reynolds number is high, viscous effects are mainly restricted to a thin *boundary layer* along the body surface, whereas viscosity can be neglected in the remaining external flowfield. As long as no massive separation occurs, both flow domains can be calculated separately by solving simplified governing equations respectively. Hereby, the inviscid outer-flow solution yields the boundary conditions to perform the subsequent boundary-layer analysis.

In this chapter the method to determine the inviscid flow about a displacment body with stern propeller is summarized whereas in Sec. 3 the boundary-layer procedure and the viscous/inviscid coupling scheme is discussed in more detail.

## 2.1 Panel Method

The inviscid flow about the airship hull is calculated using a 3D low-order panel method. With this approach an irrotational and isentropic flowfield is considered which allows to introduce a velocity potential $\Phi$. This potential consists of the known potential $\varphi_\infty$ of the undisturbed onset flow and the disturbance potential $\varphi$ caused by the submerged body.

The continuity equation represents the governing equation of the problem. For incompressible fluid this equation reads in terms of the disturbance potential as follows:

$$\Delta\varphi = \frac{\partial^2\varphi}{\partial x^2} + \frac{\partial^2\varphi}{\partial y^2} + \frac{\partial^2\varphi}{\partial z^2} = 0 \tag{6}$$

Applying Green's third identity enables to transform this Laplace-equation into the following in-

tegral equation:

$$\varphi(x,\,y,\,z) = -\frac{1}{4\pi}\iint\limits_S \frac{\sigma}{r}\,dS + \frac{1}{4\pi}\iint\limits_S \mu\vec{n}\cdot\nabla\left(\frac{1}{r}\right)dS \tag{7}$$

Hereby, $\sigma$ represents a source and $\mu$ a doublet singularity distribution on the solid body surface. For non-lifting cases, as considered in the present investigations, the use of a source distribution is sufficient. To solve the above integral equation, the external NEUMANN boundary-condition is applied. This condition implies that the velocity normal to the surface has to vanish. Since the velocity is given by the derivative of the potential, this condition can be written as:

$$\left(\vec{v}\cdot\vec{n}\right)\big|_{\text{surface}} = \Big((\nabla\Phi)\cdot\vec{n}\Big)\Big|_{\text{surface}} = 0 \tag{8}$$

To enable a numerical solution of Eq. (7) the body surface is discretized into flat quadrilateral *panels* with piecewise constant source strength. The discretisation finally yields a linear equation system to solve for the unknown source strengths $\vec{\sigma}$:

$$\begin{aligned}\big[AIC\big]\cdot\vec{\sigma} &= \overrightarrow{RHS}\\ \overrightarrow{RHS} &= -\vec{U}_\infty\cdot\vec{n}\end{aligned} \tag{9}$$

$\big[AIC\big]$ is the matrix of the aerodynamic influence coefficients which give the induction of one source panel of unit strength onto the collocation point of another panel. The components of the vectors $\vec{\sigma}$ and $\overrightarrow{RHS}$ represent the corresponding values for a particular panel $k$.

Once the source strengths are known, the inviscid velocity vector at an arbitrary field point and especially on the surface can be determined. Applying the BERNOULLI-equation finally gives the pressure field.

## 2.2 Propeller Model

The panel method is coupled to a model which enables to calculate the time-averaged influence of a propeller located on the body axis [7]. In this model the propeller disc is represented by a vortex sheet whereas the slipstream is modelled by a discrete number of vortex tubes of variable vorticity. Due to this representation, actually, a propeller with an infinite number of blades is modelled. However, the resulting induced velocity field coincides with the time-averaged velocities caused by a propeller with finite number of blades.

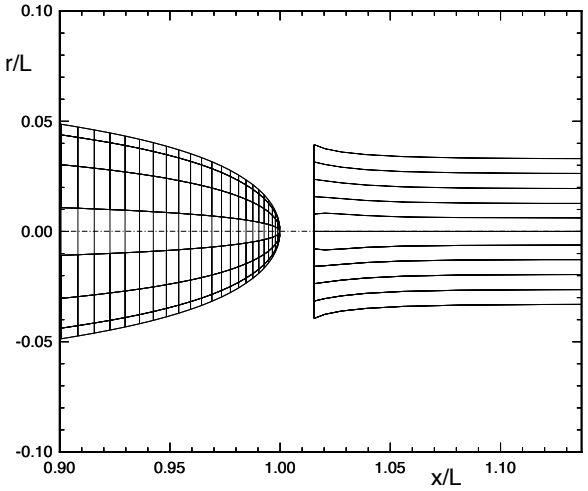


Figure 1: Calculated slipstream geometry of a propeller located downstream of a displacement body [7]

The vortex tubes in the slipstream are discretized by truncated concentric cones. Each tube is terminated by a semi-infinite vortex cylinder. The contracting slipstream geometry is determined by an iterative relaxation procedure based on the condition that the slipstream has to be force-free. This implies that the vorticity vector is parallel to the local velocity vector at each collocation point of the slipstream. With this relaxation procedure the self-influence of the propeller and its slipstream as well as the velocity field induced by a displacement body are considered.

The influence of the propeller on the hull is considered by a modification of the right-hand-side of Eq. (9). Hereby, the velocity vector induced by the propeller and its slipstream onto each panel collocation point on the hull surface is added to the undisturbed freestream velocity $\vec{U}_\infty$. Thereafter, the source distribution is recalculated to satisfy the updated right-hand-side. This alters the body-induced velocity field which requires an adaption of the slipstream geometry. This procedure is repeated until convergency is achieved. An example of a calculated fully-relaxed propeller slipstream including propeller-hull interference effects is given in Fig. 1.

The propeller thrust and the required power finally are determined by an integration of the forces acting on the bound circulation distribution. These forces are obtained from application of the

KUTTA-JOUKOWSKY-law. As a major improvement to the model described in Ref. [7] the viscous instead of the inviscid propeller onset flowfield is considered during the calculation of the propeller forces. Furthermore, the viscous drag of the propeller blades is estimated based on the drag coefficient of a flat blade with fully laminar or fully turbulent boundary layer respectively. The flat plate drag-coefficient depends on the chord REYNOLDS number $Re_c(r)$ at the particular blade section and is given by:

$$c_d|_{\text{laminar}} = \frac{1.328}{\sqrt{Re_c}} \tag{10}$$

$$c_d|_{\text{turbulent}} = \frac{2 \cdot 0.455}{log_{10}\left(Re_c\right)^{2.58}} \tag{11}$$

The consideration of the detailed aerodynamic characteristics of the blade sections will be implemented next.

It is important to mention that with the present implementation of the propeller model the bound circulation distribution on the propeller blades is *not* calculated but has to be specified by the user. This distribution might e.g. be taken from a previously performed propeller design, from experiments or from the known distribution of 'ideal' isolated propellers. An extension of the model to theoretically predict the circulation distribution during the coupled analysis will be investigated in future.

# 3 Calculation of the Viscous Flow About the Airship Hull

## 3.1 Boundary-Layer Procedure

### Governing Equations and Integral Boundary-Layer Parameters

For the present investigations a first-order integral boundary-layer procedure was applied to calculate the viscous effects along the hull. The method is based on the numerical integration of the integral momentum and energy equations. In a surface-oriented coordinate system (Fig. 2) these equations read for incompressible axisymmetrical flows as follows:

$$\frac{d\delta_2}{ds} + \delta_2 \left[ \left( \frac{H_{12}+2}{U_e} \right) \frac{dU_e}{ds} + \frac{1}{R}\frac{dR}{ds} \right] = \frac{c_f}{2} \tag{12}$$

$$\frac{d\delta_3}{ds} + \delta_3 \left[ \frac{3}{U_e}\frac{dU_e}{ds} + \frac{1}{R}\frac{dR}{ds} \right] = c_D \tag{13}$$

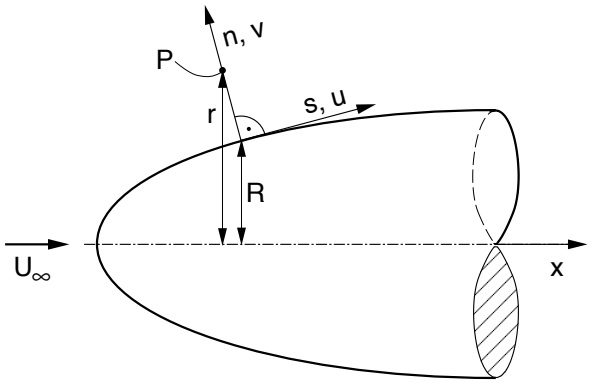


Figure 2: Surface-oriented coordinate system used for the calculation of axisymmetric boundary layers

These governing equations also hold for $\delta_2 \not\ll R$ if the integral parameters according to the following *axisymmetric* definitions are presumed:

$$\delta_1 = \int_0^\delta \left[ 1 - \frac{u(n)}{U_e} \right] \left( 1 + n\,\kappa \right) dn \tag{14}$$

$$\delta_2 = \int_0^\delta \frac{u(n)}{U_e} \left[ 1 - \frac{u(n)}{U_e} \right] \left( 1 + n\,\kappa \right) dn \tag{15}$$

$$\delta_3 = \int_0^\delta \frac{u(n)}{U_e} \left[ 1 - \left( \frac{u(n)}{U_e} \right)^2 \right] \left( 1 + n\,\kappa \right) dn \tag{16}$$

$$\text{with} \quad \kappa = \sqrt{\frac{1}{R^2} - \left( \frac{1}{R}\frac{dR}{ds} \right)^2} \tag{17}$$

In contrast the integral parameters according to the *plane* definition are denoted $\overline{\delta}_1$, $\overline{\delta}_2$ and $\overline{\delta}_3$ with:

$$\overline{\delta}_1 = \int_0^\delta \left[ 1 - \frac{u(n)}{U_e} \right] dn \tag{18}$$

$$\overline{\delta}_2 = \int_0^\delta \frac{u(n)}{U_e} \left[ 1 - \frac{u(n)}{U_e} \right] dn \tag{19}$$

$$\overline{\delta}_3 = \int_0^\delta \frac{u(n)}{U_e} \left[ 1 - \left( \frac{u(n)}{U_e} \right)^2 \right] dn \tag{20}$$

The system of ordinary differential equations (12), (13) is closed by three algebraic relations to solve for the five unknown integral parameters $\delta_1$, $\delta_2$, $\delta_3$, $c_f$ and $c_D$. With the present

method the closure relations proposed by Eppler [1] are used. These closure conditions were derived from Falkner-Skan self-similar profiles for laminar boundary layers whereas empirical relations were correlated for turbulent flows. The complete system of equations is solved for the dependent parameters $\delta_2$ and $\delta_3$ based on the velocity distribution along the boundary-layer edge $U_e(s)$ resulting from the inviscid outer-flow computation.

#### Transition Prediction

The location of the laminar to turbulent transition can be either specified by the user or predicted by a local empirical criterion [1] or a semi-empirical $e^n$-method. If laminar separation occurs upstream of transition it is switched to turbulent closure relations at the separation point.

In the present investigations the $e^n$-method was applied to recalculate wind-tunnel experiments featuring natural transition. The $e^n$-approach takes advantage of the fact that the transition process in subsonic 2D-flows is typically associated with the growth and breakdown of Tollmien-Schlichting waves (TS-waves). As long as the disturbance amplitude $A$ is small enough, the amplification can be predicted by means of linear stability theory. The basic idea of the $e^n$-method is that transition may be assumed when the most amplified frequency reaches a certain critical amplification factor $n_{crit.} = \ln(A_{crit.}/A_{initial})$. The value of $n_{crit.}$ depends on freestream conditions, the receptivity mechanism and on the definition of the transition 'point'. With the present $e^n$-approach, spatial disturbance growth is considered. To minimize the computational effort a database method was implemented as an alternative to a direct solution of the Orr-Somerfeld equation. More details along with validation examples are given in Refs. [6], [8] and [9].

#### Drag Prediction

To determine the viscous drag of the hull the well-known Squire-Young formula is applied. This approach is based on the evaluation of the calculated momentum thickness at the stern and accounts for the skin-friction as well as for the form drag of the boundary layer. If the propeller is switched on, the propeller-induced pressure drag is calculated from an integration of the pressure distribution along the hull surface. The sum of both contributions represents the total hull drag.

### 3.2 Viscous/Inviscid Coupling

With the theoretical model described so far, the inviscid velocity distribution $U_e(s)$ along the hull surface is specified as boundary condition for the boundary-layer calculation. This gives the correct result only for the asymptotic condition of infinite REYNOLDS number and vanishing boundary-layer thickness. For practical problems with finite values of $Re$ the displacement effect of the boundary layer affects the outer flow and thus the distribution $U_e(s)$. This, in turn, has an impact on the boundary-layer development. The displacement effect is most pronounced in the pressure recovery region near the tail. Therefore, an iterative coupling of the boundary layer and the outer-flow computation is needed if realistic boundary-layer properties in the stern region of the hull are of interest. The objective, hereby, is to modify the inviscid flow calculation in such a way that it provides the correct velocity distribution $U_e$ along the outer edge of the boundary layer under consideration of its displacement effect. We shall call this *equivalent inviscid flow computation* [4].

#### Transpiration Technique

In principle, two different coupling schemes are possible. With the *solid displacement surface model* the calculated displacement thickness is added to the solid hull shape to find the relevant contour for the subsequent outer-flow computation. The main disadvantage of this approach is that the geometry-dependent aerodynamic influence coefficients $[AIC]$ have to be recalculated during every iteration step, which is rather time-consuming.

For this reason the *surface transpiration model* is usually preferred. With this second approach an additional source-singularity distribution on the surface of the solid hull shape is introduced to simulate the boundary-layer displacement effect. For this purpose the right-hand-side of the linear equation system (9) is modified by adding a *transpiration velocity* $v_n$.

At a certain position on the hull the transpiration velocity can be derived from an integration of the continuity equation across the boundary layer for both, the real viscous flow and the equivalent inviscid flow. The value of $v_n$ can be determined from the fact that the mass flow normal to the wall (caused by $v_n$) in the equivalent inviscid flow has to be equal to the streamwise rate of change of the

mass flow deficit in the boundary layer [4]. For incompressible axisymmetrical flows it follows:

$$v_n = \frac{d(U_e \cdot \delta_1)}{ds} + \frac{U_e \cdot \delta_1}{R} \cdot \frac{dR}{ds} \qquad (21)$$

During the present investigations it has shown that in some cases Eq. (21) yields small irregularities of the $v_n$-distribution in the vicinity of the stern. An improvement, i.e. a smoother $v_n$-distribution was achieved by introducing the integral momentum equation (12) into Eq. (21) which finally gives:

$$v_n = U_e \left( \frac{d\delta_1}{ds} + H_{12}\frac{c_f}{2} - H_{12}\frac{d\delta_2}{ds} - \frac{H_{12}\delta_1}{U_e}\frac{dU_e}{ds} - \frac{\delta_1}{U_e}\frac{dU_e}{ds} \right) \qquad (22)$$

If the full transpiration velocity as resulting from Eq. (21) or (22) is added to the right-hand-side of Eq. (9) severe stability problems arise: Near the tail region of an axisymmetric body a strong flow deceleration results from the first inviscid flow analysis. Along with the reducing body radius, an unrealistic strong growth of the displacement thickness is predicted by the subsequent boundary-layer calculation. According to Eq. (21) this yields to very high values for $v_n$ in the tail region. As a consequence, the beginning of the pressure recovery is shifted in upstream direction during the next iteration loop (Fig. 3) which in turn causes an earlier growth of the boundary layer. Usually an unstable or a divergent behaviour of the viscous/inviscid coupling process results.

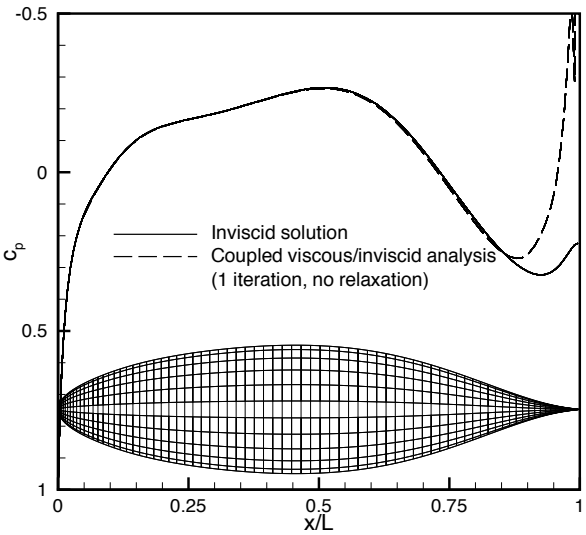


Figure 3: Unstable behaviour of the viscous/inviscid coupling process without relaxation, 'Lotte' hull, $Re_L = 16 \cdot 10^6$, $x_{tra}/L = 0.05$

## Under-Relaxation Scheme and Determination of the Relaxation Factor

To obtain a stable behaviour of the coupling process, only a part $\omega$ of the theoretical update of $v_n$ may be added to the right-hand-side of Eq. (9), i.e. an under-relaxation scheme has to be introduced. Usually the relaxation factor $\omega$ is chosen empirically. For the present investigations a more sophisticated approach was applied which is based on a local linear stability analysis of the coupled process as proposed by Le Balleur [3] (see also Lock [4]). Following the derivation of an 'optimum' relaxation factor for plane flows as given by Lock [4] an analogous theory will now be derived for axisymmetrical boundary layers along a body with locally cylindrical shape.

First of all, the transpiration velocity $v_n$ according to Eq. (21) is nondimensionalized with the outer-flow velocity $U_e$:

$$\Sigma = \frac{v_n}{U_e} \qquad (23)$$

The quantities $\Sigma^{(n)}$, $v_n^{(n)}$ and $U_e^{(n)}$ shall denote the flow properties at the $n$-th iteration whereas $\widetilde{\Sigma}$, $\widetilde{v}_n$ and $\widetilde{U}_e$ represent the correct final values after convergency of the iteration process. To define the discrepancy from the converged solution the following error functions are introduced:

$$\sigma^{(n)} = \Sigma^{(n)} - \widetilde{\Sigma} \qquad (24)$$

$$u^{(n)} = \frac{U_e^{(n)} - \widetilde{U}_e}{\widetilde{U}_e} \qquad (25)$$

We assume that the rate of change of any flow property is negligibly small compared to the variation of the above error-functions. Then, a locally linearized analysis of the behaviour of $u$ and $\sigma$ can be performed. To describe the equivalent inviscid flow a potential function is introduced which satisfies the LAPLACE-equation in case of incompressible fluids. In cylindrical coordinates this equation reads as follows:

$$\Phi_{xx} + \Phi_{rr} + \frac{1}{R}\Phi_r = 0 \qquad (26)$$

If, furthermore, the crude assumption is met that the analysed body has locally a cylindrical shape[2], the outer-edge velocity is oriented in axial and the transpiration velocity in radial direction which allows to determine the error-functions as follows:

$$u = \frac{\partial \Phi}{\partial x} = \Phi_x \tag{27}$$

$$\sigma = \frac{\partial \Phi}{\partial r} = \Phi_r \tag{28}$$

The error-functions $u$ and $\sigma$ are coupled by the LAPLACE-equation (26) and, on the other hand, by the boundary-layer equations via Eq. (21).

Eq. (26) is now represented by a superposition of harmonic waves, i.e. a FOURIER-expansion is introduced in order to investigate the amplification of particular waves of the errors in downstream direction. It can easily be shown that a solution of Eq. (26) for a wave number $\nu = \frac{2\pi}{\lambda}$ is given by:

$$\Phi(x,r) = A \cdot e^{i\nu x} \cdot e^{-\kappa(r-R)} = A \cdot f(x) \cdot g(r) \tag{29}$$

$$\text{with:} \quad \kappa = \frac{\frac{1}{R} + \sqrt{\frac{1}{R^2} + 4\nu^2}}{2} \quad \text{and} \quad i = \sqrt{-1} \tag{30}$$

For the partial derivatives it follows:

$$u = A \cdot i\nu\, e^{i\nu x} \cdot g(r) = A \cdot i\nu f(x) \cdot g(r) \tag{31}$$

$$u_x = \frac{\partial u}{\partial x} = -A \cdot \nu^2 f(x) \cdot g(r) \tag{32}$$

$$\sigma = A \cdot f(x) \cdot g_r(r) \tag{33}$$

Combining Eqs. (32) and (33) yields:

$$u_x = -\nu^2 \sigma \frac{g(r)}{g_r(r)} = \frac{\nu^2 \sigma}{\kappa} \tag{34}$$

Now, the dependency of the nondimensionalized transpiration velocity $\Sigma = \frac{v_n}{U_e}$ on the velocity gradient $\frac{dU_e}{ds}$ resulting from the *viscous* analysis shall be derived. For this purpose the gradient $\frac{d\delta_1}{ds}$ is eliminated in Eq. (21) by inserting the integral boundary-layer equations (12) and (13). Rearranging the resulting expression finally yields:

$$\Sigma = \frac{v_n}{U_e} = \frac{dU_e}{ds}\frac{\delta_2}{U_e} B + C \tag{35}$$

$$\text{with} \quad B = \Big[ \quad H_{12} - 3\, H_{32} \frac{dH_{12}}{dH_{32}} - (H_{12}+2)\left(H_{12} - H_{32}\frac{dH_{12}}{dH_{32}}\right)\Big] \tag{36}$$

$$\text{and} \quad C = \left(H_{12} - H_{32}\frac{dH_{12}}{dH_{32}}\right)\left(\frac{c_f}{2} - \frac{\delta_2}{R}\frac{dR}{ds}\right) + \frac{dH_{12}}{dH_{32}}\left(c_D - \frac{\delta_3}{R}\frac{dR}{ds}\right) + \frac{\delta_1}{R}\frac{dR}{ds} \tag{37}$$

The derivative of the shape factor $\frac{dH_{12}}{dH_{32}}$ can be determined from the closure relations used [1] in analytical form.

Introducing the error-functions (24) and (25) into Eq. (35), taking into account that the derivatives of the flow properties are assumed to be small and that $\frac{dU_e}{ds} = \frac{dU_e}{dx}$ for the flow direction considered, it follows:

$$\sigma = \frac{du}{dx} \cdot \delta_2\, B = B\, \delta_2 \cdot u_x \tag{38}$$

During the viscous/inviscid coupling the transpiration velocity for the next iteration $(n+1)$ is calculated based on the velocity gradient of the $n$-th iteration. Thus:

$$\sigma^{(n+1)} = B\, \delta_2 \cdot u_x^{(n)} \tag{39}$$

Inserting Eq. (34) as resulting from the evaluation of the LAPLACE-equation into (39) shows how the error $\sigma$ behaves from one iteration of the viscous/inviscid coupling to the next:

$$\sigma^{(n+1)} = \mu\, \sigma^{(n)} \tag{40}$$

$$\text{with} \qquad \mu = \frac{B\delta_2\nu^2}{\kappa} \tag{41}$$

with $\mu$ representing an amplification factor. Note that the error in the transpiration velocity is amplified for $|\mu| > 1$. In this case it can be expected that the viscous/inviscid coupling will show an unstable behaviour and that an under-relaxation has to be introduced to stabilize the process.

Now a relation to determine a suitable relaxation factor $\omega$ shall be derived. Rewriting the error-function $\sigma$ for iteration step $(n)$ and $(n+1)$ and

[2] An analogous theory was develeoped for a locally conical body shape. Both approaches yield almost identical results with respect to the calculated relaxation factor, see Fig. 6. For simplicity only the cylindrical approach is reported in the present paper.

solving for the converged solution $\widetilde{\Sigma}$ allows to eliminate $\sigma$ if Eq. (40) is inserted:

$$\widetilde{\Sigma} = \Sigma^{(n)} - \sigma^{(n)}$$

$$\text{and} \qquad \widetilde{\Sigma} = \Sigma^{(n+1)} - \sigma^{(n+1)} = \Sigma^{(n+1)} - \mu\,\sigma^{(n)}$$

$$\Rightarrow \qquad \widetilde{\Sigma} = \frac{\mu}{\mu-1}\Sigma^{(n)} - \frac{1}{\mu-1}\Sigma^{(n+1)} \tag{42}$$

This equation states that the *converged* value of the transpiration velocity can, in principle, be determined from the values $\Sigma^{(n)}$ and $\Sigma^{(n+1)}$ of two subsequent iterations. Because of the simplifying assumptions introduced during the derivation, Eq. (42) can only be expected to give an estimate. Nevertheless, it might be used to obtain an 'optimum' relaxation factor $\omega$. Rearranging Eq. (42) yields:

$$\widetilde{\Sigma} = \Sigma^{(n)} + \omega\,\left(\Sigma^{(n+1)} - \Sigma^{(n)}\right) \tag{43}$$

$$\text{with} \qquad \omega = \frac{1}{1-\mu} = \frac{1}{1-\frac{B\delta_2\nu^2}{\kappa}} \tag{44}$$

In the above equation no statement about the wave number $\nu$ was made so far. To specify the value of $\nu$ it should be mentioned that with a numerical method at least two nodes within one wavelength are needed to resolve a harmonic wave. For the panel method this means that the highest wave number $\nu_{max}$ which can result for the error $u$ is determined by the distance $\Delta s$ between the neighbouring panel collocation points. With

$$\nu_{max} \approx \frac{\pi}{\Delta s} \tag{45}$$

a reasonable minimum for the 'optimum' relaxation factor is given by:

$$\omega_{opt} = \frac{1}{1-\frac{B\delta_2}{\kappa}\left(\frac{\pi}{\Delta s}\right)^2} \tag{46}$$

This equation can be applied locally at each panel collocation point along the hull surface to obtain a distribution for the relaxation factor $\omega_{opt}(s)$. It was used in the present investigations to stabilize the viscous/inviscid coupling process and yields most often good convergence characteristics. Nevertheless, in some particular cases, the coupling process tends to become unstable after convergency seemed to have been achieved. In those cases the relaxation factor was attenuated.

## Discussion of the Parameters Affecting the Relaxation Factor

Since $B$ (Eq. (36)) is always negative, at least for the closure relations used in the present boundary-layer method, Eq. (46) shows that smaller relaxation factors are needed (compare discussion of Lock [4]):

- ... for higher $\delta_2$-values, i.e. for lower REYNOLDS-numbers
- ... for smaller values of $\Delta s$, i.e. for finer panel meshes
- ... for higher absolute values of $B$

The evaluation of the shape factor relations used shows that the module of $B$ becomes larger as $H_{32}$ decreases, see Fig. 4. Therefore, small values of $\omega$ are required in the vicinity of separation.

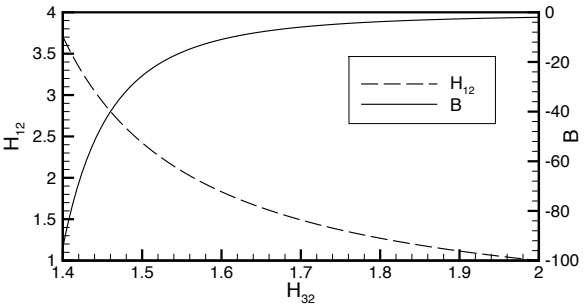


Figure 4: Shape factor relation for turbulent 2D boundary-layers according to Eppler [1] and resulting behaviour of the parameter $B$

## Application Example of the Coupling Scheme

As an example the analysis of the 'Lotte' hull given in Fig. 3 was repeated using the present relaxation scheme. The pressure distribution obtained after 20 iterations along with the inviscid result is depicted in Fig. 5. No tendency to an unstable behaviour could be observed and the solution was practically converged after 20 iteration cycles. Fig. 6 shows the distribution of the 'optimum' relaxation factor after the first iteration step. It can be seen that in the nose region almost no underrelaxation is needed whereas very small values of $\omega$ result near the tail for the reasons discussed above. For comparison, the $\omega$-distribution which would result if a locally conical body shape is assumed during the derivation of $\omega_{opt}$, is also depicted in Fig. 5.

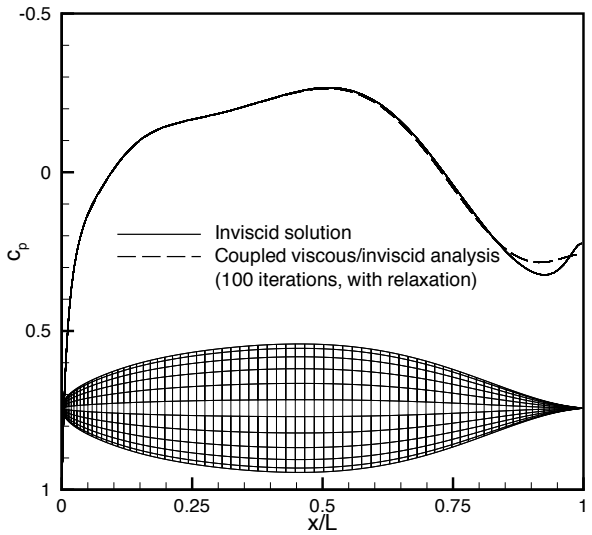


Figure 5: Viscous/inviscid coupling with relaxation, Lotte hull, $Re_L = 16 \cdot 10^6$, $x_{tra}/L = 0.05$

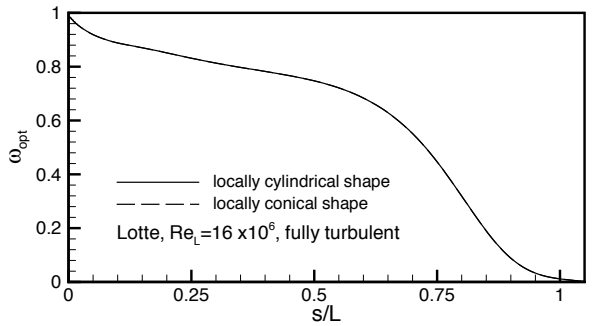


Figure 6: Distribution of the 'optimum' relaxation factor $\omega_{opt}$ according to Eq. (46), Lotte hull, $Re_L = 16 \cdot 10^6$, fully turbulent boundary layer, first iteration

Since the curves practically coincide the approach described in the present paper is regarded to be sufficient and was therefore used for all subsequent calculations.

## 3.3 Derivation of the Boundary-Layer Profiles from Integral Parameters

With an integral boundary-layer procedure no information about the detailed velocity distribution across the boundary layer is provided. To obtain the viscous onset-flow velocity field for the stern propeller, the boundary-layer profile $\frac{u}{U_e}(r, L)$, therefore, has to be determined from the calculated axisymmetric integral parameters like $\delta_1(L)$, $\delta_2(L)$ or $\delta_3(L)$.

### Representation of Turbulent Boundary-Layer Profiles

For plane flows several families of velocity profiles are well established like the FALKNER-SKAN self-similar profiles for laminar boundary layers. For turbulent flows some analytical expressions are known. A rather simple representation is given by the power-law profiles:

$$\frac{u}{U_e} = \left(\frac{n}{\delta}\right)^a \tag{47}$$

Swafford and Whitfield [12] proposed an analytical expression to describe incompressible attached or separated turbulent boundary layers. This approach is more physically motivated and takes the zonal character of turbulent boundary layers into consideration:

$$\frac{u}{U_e} = \frac{u_\tau}{U_e} sign(c_f) \frac{\arctan\left(0.09 y^+\right)}{0.09} + \left(1 - \frac{u_\tau}{U_e} \frac{\pi sign(c_f)}{0.18}\right) \tanh^{\frac{1}{2}}\left(a \left(\frac{n}{\overline{\delta}_2}\right)^b\right) \tag{48}$$

$$\text{with} \qquad u_\tau = U_e \cdot \sqrt{\left|\frac{c_f}{2}\right|} \tag{49}$$

$$\text{and} \qquad y^+ = \frac{u_\tau n}{\nu} = Re_{\overline{\delta}_2} \cdot \frac{u_\tau}{U_e} \cdot \frac{n}{\overline{\delta}_2} \tag{50}$$

Notice that the momentum thickness $\overline{\delta}_2$ according to the plane defintion (19) has to be used when evaluating Eq. (48). The parameters $a$, $b$ are constant across the boundary-layer profile but are dependent on its shape and thus have to be determined for each profile considered. For this purpose, ansatz (48) is introduced into the definitions (14), (15) and (16) to solve for $\delta_1$, $\delta_2$, $\delta_3$ by numerical integration. The corresponding shape factors $H_{12}$ and $H_{32}$ have to be equal to the specified values. These compatibility equations enable the determination of the parameters $a$, $b$ by solving a nonlinear equation system, e.g. using a damped NEWTON-RAPHSON method.

The profile families discussed might also be used to represent the velocity distribution across axisymmetric boundary layers as long as its thickness is moderate.

Now it shall be described how to obtain the exponent $a$ of the power-law profiles and the relevant boundary-layer thickness $\delta$ from given values $\delta_1$ and $\delta_2$ as resulting from the axisymmetric boundary-layer calculation. First of all, ansatz

(47) is introduced into Eqs. (14) and (15) which yields:

$$\frac{\delta_1}{\delta} = 1 - \frac{1}{a+1} + \frac{\kappa\,\delta}{2} - \frac{\kappa\,\delta}{a+2} \tag{51}$$

$$\frac{\delta_2}{\delta} = \frac{1}{a+1} - \frac{1}{2a+1} + \kappa\,\delta\left(\frac{1}{a+2} - \frac{1}{2a+2}\right) \tag{52}$$

Since $\frac{\delta_1/\delta}{\delta_2/\delta} = \frac{\delta_1}{\delta_2} = H_{12}$ which is known from the boundary-layer calculation and $\kappa$ from the geometric properties of the analyzed body, Eqs. (51) and (52) yield a first equation to determine $a$ and $\delta$:

$$\begin{aligned}&\frac{H_{12}+1}{a+1} + \frac{\kappa\,\delta\,(H_{12}+1)}{a+2}\\ &-\frac{H_{12}}{2a+1} - \frac{H_{12}\,\kappa\,\delta}{2a+2} - \frac{2+\kappa\,\delta}{2} = 0\end{aligned} \tag{53}$$

Rearranging Eq. (51) gives the second equation required:

$$\delta = \sqrt{\frac{(a+2)^2}{\kappa^2(a+1)^2} + \frac{2(a+2)}{\kappa\,a}\cdot\delta_1} - \frac{a+2}{\kappa(a+1)} \tag{54}$$

The coupled equations (53) and (54) can be solved iteratively using a NEWTON method.

With the known values of $a$ and $\delta$ the velocity distribution $\frac{u}{U_e}(n)$ across the boundary layer can finally be obtained from ansatz (47).

To give an example, Fig. 7 shows the approximation of measured boundary-layer profiles [11] by the profile families discussed. The power-law profiles were determined from measured values of $\overline{\delta}_1$ and $\overline{\delta}_2$ whereas $Re_{\overline{\delta}_2}$ and $c_f$ are required additionally to derive the Swafford profiles. Both approaches are in good agreement to the actual velocity distributions even though very thick boundary layers near the stern of an axisymmetric body were considered. It is, therefore, expected that with the present post-processing approach the propeller onset-flow velocity field is determined to sufficient accuracy as long as the coupled viscous/inviscid calculation yields reliable results for the integral boundary-layer parameters. For the present investigations the power-law approach is used to obtain the boundary-layer profile at the stern of the hull.

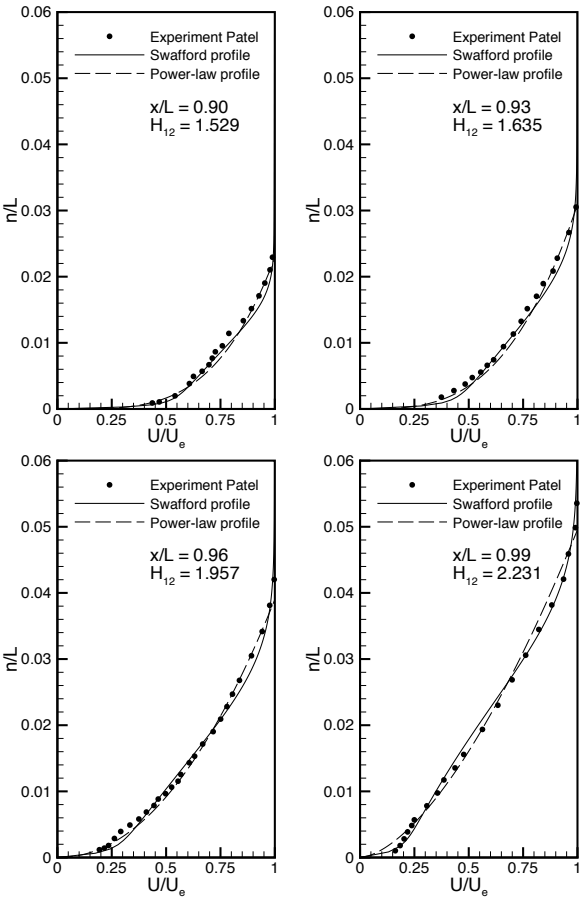


Figure 7: Approximation of boundary-layer profiles based on measured integral parameters, experiment by Patel et al. [11]

## Convertion of Integral Boundary-Layer Parameters from Axisymmetric to Plane Definition

Besides the approximation of turbulent boundary-layer properties, the power-law ansatz enables a simple convertion of the axisymmetric integral parameters $\delta_1$, $\delta_2$, $\delta_3$ into the properties $\overline{\delta}_1$, $\overline{\delta}_2$, $\overline{\delta}_3$ according to the plane definition. Inserting Eq. (47) into definitions (18) to (20) yields:

$$\overline{\delta}_1 = \left(1 - \frac{1}{a+1}\right)\cdot\delta \tag{55}$$

$$\overline{\delta}_2 = \left(\frac{1}{a+1} - \frac{1}{2a+1}\right)\cdot\delta \tag{56}$$

$$\overline{\delta}_3 = \left(\frac{1}{a+1} - \frac{1}{3a+1}\right)\cdot\delta \tag{57}$$

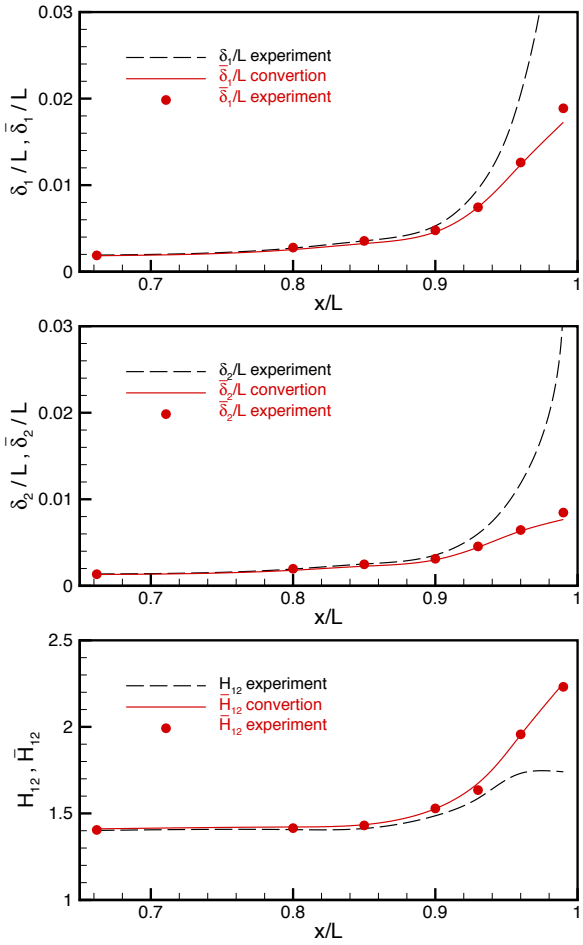


Figure 8: Convertion of displacement thickness $\delta_1$, momentum thickness $\delta_2$ and shape factor $H_{12}$ from axisymmetric to plane definition using the power-law approach

Fig. 8 is to demonstrate the capability of the power-law approach to be used for convertion of the integral boundary-layer parameters. Based on measured values [11] of $\delta_1$ and $\delta_2$ Eqs. (53) to (56) were applied to theoretically determine the corresponding values $\overline{\delta}_1$, $\overline{\delta}_2$ and $\overline{H}_{12}$. The obtained distributions almost coincide with the experimental results.

# 4 Results and Discussion

## 4.1 Viscous Flow about the Hull without Propeller Influence

Detailed experiments on axisymmetric bodies with stern propellers are hardly available in literature open to the public. Therefore, the present theoretical model is at first validated for the bare hull with respect to the boundary-layer calculation and the viscous/inviscid coupling scheme described. For this purpose low REYNOLDS-number experiments were selected because for these conditions the boundary layer in the tail region is rather thick and viscous/inviscid interaction effects are most pronounced. Thus, limitations of the first-order boundary-layer procedure and the coupling scheme become more obvious than for the high REYNOLDS-numbers of real airships.

As very first example, Fig. 9 shows the calculated and the measured pressure distribution for a 1 : 20 scale model of the remote-controlled airship 'Lotte' built at the University of Stuttgart. The experiments were performed in the 'Medium Wind-Tunnel' of the IAG with a turbulence lattice being mounted in some distance upstream of the model. The lattice increases the turbulence factor to $Tu \approx 0.06$ which yields an almost fully turbulent flow about the entire hull like it is true for full-scale airships. The wind-tunnel model was supported by a tailboom which was also considered in the calculation.

It is obvious that in the tail region the inviscid pressure distribution strongly deviates from the measured distribution due to the neglection of the boundary-layer displacement effect. The present coupled viscous/inviscid analysis is in good agreement with the experiments even though the theoretical result shows a slightly stronger pressure recovery. However, it should be noticed that the calculation yields the surface pressure for the equivalent inviscid flow. This pressure differs from that of the real viscous flow if, due to curvature effects, the pressure is not constant across the boundary layer [4]. This is expected to be true in the tail region of the analyzed body at least for the low REYNOLDS numbers considered.

The boundary-layer experiments performed by Patel et al. [11] were chosen as second example. The examined shape is a 1:6 ellipsoid with a conical tail piece (Fig. 10) which yields a strong thickening of the boundary layer in this area. This test case represent a tough challenge for the viscous/inviscid

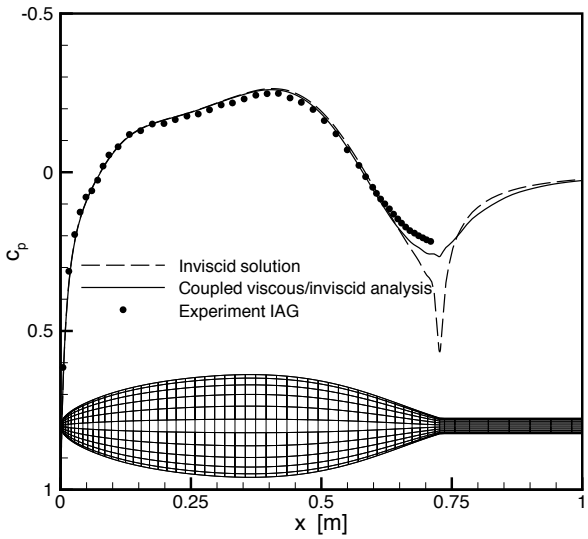


Figure 9: Surface pressure distribution about a model of the 'Lotte'-hull with tail-boom, experiment by Lowag & Funk [5], $Re_L = 1.3 \cdot 10^6$, $\alpha = 0°$, fully turbulent

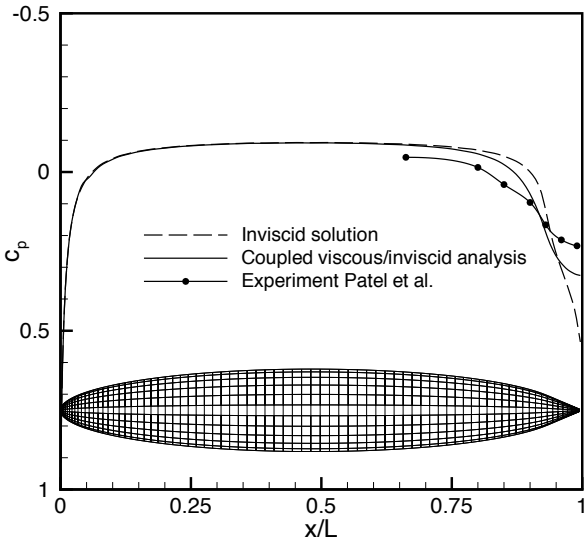


Figure 10: Surface pressure distribution along a body of revolution, experiment by Patel et al. [11], $Re_L = 1.26 \cdot 10^6$, forced transition at $x_{tra}/L = 0.05$

coupling since it was especially designed to investigate strong interaction effects between boundary layer and external flow.

The strong interaction causes a significant reduction of the measured pressure recovery in comparison to the inviscid solution, see Fig. 10. The coupled viscous/inviscid analysis yields a correct

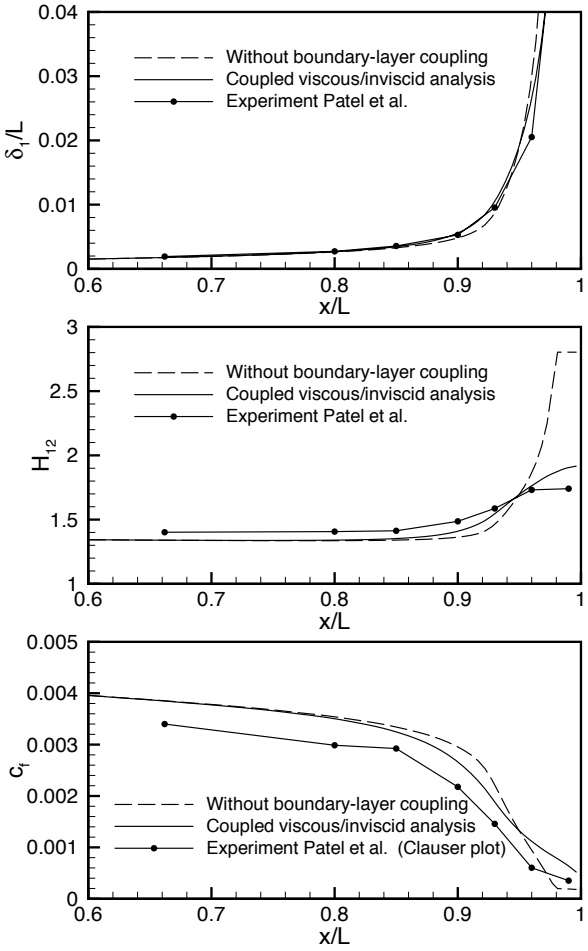


Figure 11: Distributions of the displacement thickness $\delta_1$, the shape factor $H_{12}$ and the skin-friction coefficient $c_f$ along the body of revolution examined by Patel [11], $Re_L = 1.26 \cdot 10^6$, $\alpha = 0°$, forced transition at $x_{tra}/L = 0.05$

tendency but again, the recompression is overpredicted.

Fig. 11 gives the results of calculated and measured boundary-layer parameters. The coupled analysis shows a rather good agreement with the experiments even in the vicinity of the pointed tail. Notice, that the calculation without coupling gives significant different results for the shape factor distribution. If the displacement effect is neglected a steep increase of $H_{12}$ in the tail region along with turbulent separation at $x_{sep}/L \approx 0.98$ can be observed. On the other hand, the coupled analysis as well as the experiment give substantial lower $H_{12}$-values and no separation occurs.

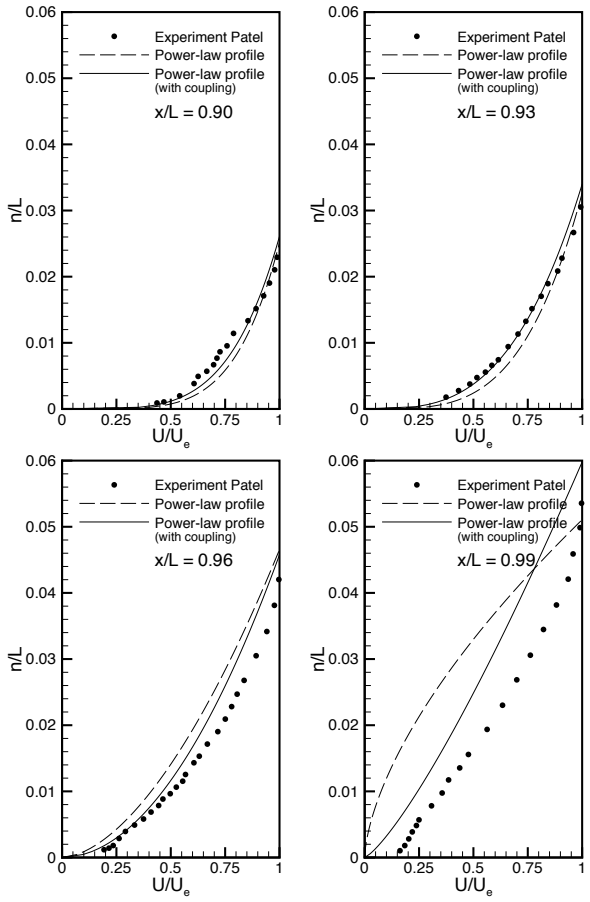


Figure 12: Predicted and measured boundary-layer profiles for the body of revolution examined by Patel [11], $Re_L = 1.26 \cdot 10^6$, $\alpha = 0°$, forced transition at $x_{tra}/L = 0.05$

Fig. 12 finally shows the comparison of measured boundary-layer profiles and power-law profiles determined from the calculated integral parameters (compare Sec. 3.3). The velocity profiles as resulting from a coupled analysis yield a pretty good match to the real profiles except for the most downstream measuring location $x/L = 0.99$. At the stern the inner region of the boundary layer could not satisfactory represented by the one-parameter power-law approach and, furthermore, the boundary-layer thickness is slightly overpredicted. Nevertheless, it becomes obvious that a viscous/inviscid coupling is indispensable to predict reasonable boundary-layer properties in the tail region.

Because for real airships the REYNOLDS-number is much higher than for the test cases considered, the displacement effect is less pronounced and it can be expected that the present model enables the calculation of the viscous flowfield to sufficient accuracy for the intended investigations on stern propellers.

## 4.2 Efficiency of Stern-Mounted Propellers

Because it is instructive for the study of the propeller-hull interference effects, calculation results for the 'Lotte' airship with stern propeller as reported in Ref. [7] are depicted once more and compared to results obtained with the present enhanced theory (Fig. 13). The full-scale airship of length $L = 16m$ was examined for a flight speed of $U_\infty = 15m/s$ which corresponds to a REYNOLDS-number of $Re_L = 16 \cdot 10^6$. The hull boundary-layer was assumed to be fully turbulent. To enable a comparison to previous results, the bound circulation distribution derived from the experiments of Hucho [2] was specified even though the actual Lotte propeller shows a different design. During the calculation the propeller rotational speed was iterated until the obtained thrust was equal to the viscous plus the propeller-induced hull drag.

In Ref. [7] the influence of the distance between propeller and stern on thrust coefficient $c_T$, power coefficient $c_P$ and efficiency $\eta$ was investigated. With these earlier calculations only the *inviscid* flow field was considered during the analysis of the propeller characteristics. Due to the propeller-induced hull drag the thrust required for steady flight increases when the propeller approaches the stern, see Fig. 13. As discussed in Ref. [7] the propeller efficiency increases accordingly because the onset-flow velocity of the propeller decreases in the vicinity of the displacement body. Altogether, the required power which is the relevant quantity to rate the propulsive efficiency remains almost constant if the viscous hull wake is not considered.

With the extended calculation method described in Chapter 3 the influence of the *viscous* hull wake on the characteristics of a stern-mounted propeller can be quantified. The obtained results are given in Fig. 13 by symbols. It is obvious that the required power is significantly reduced compared to the previous results whilst the thrust is almost unaffected. The propeller efficiency (based on $U_\infty$) increases accordingly and is well above 100% ($\eta \approx 1.1$ assuming a fully laminar and $\eta \approx 1.3$ for

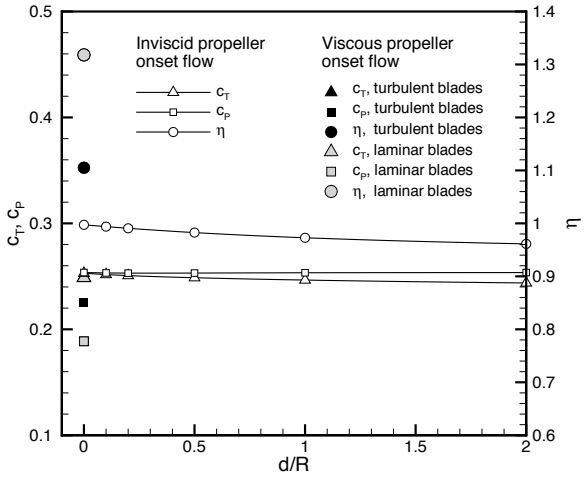


Figure 13: Influence of viscous effects on thrust resp. power coefficient and efficiency of a stern propeller (viscous results according to present theory, inviscid results as given in Ref. [7]), Lotte hull, $Re_L = 16 \cdot 10^6$, $\alpha = 0°$, forced transition at $x_{tra}/L = 0.05$

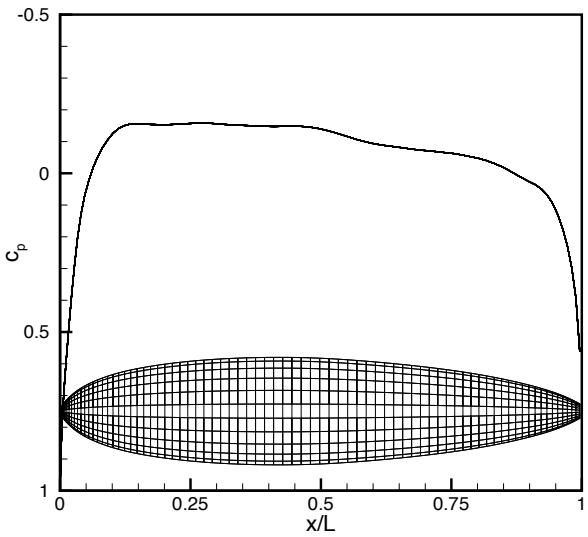


Figure 14: Inviscid pressure distribution along an airship hull investigated by McLemore [10], $\alpha = 0°$

a fully turbulent blade boundary-layer). It should be mentioned that these values strongly depend on the specified bound circulation distribution and are, therefore, only valid for the particular considered distribution. Nevertheless it becomes obvious that the gain in efficiency overcompensates the propeller-induced drag and that an adequately designed stern propeller is a very favourable propulsion device for airships.

As another example, an attempt was made to recalculate the experiments on an airship model with stern-propeller performed by McLemore [10]. For this purpose the shape of the airship hull depicted in report [10] was at first digitized and slightly smoothed. This contour along with the inviscid pressure distribution is given in Fig. 14. With the present calculations the bare hull at zero incidence was analyzed whereas the experiments were performed for the complete configuration with fins and gondola.

Since the actual bound circulation distribution of the stern propeller is not reported in Ref. [10], again, the qualitative distribution resulting from experiments of Hucho [2] was specified. The absolute level of the circulation strength was scaled such that a thrust coefficient of $c_T = 0.04$ was obtained for the same advance ratio $\lambda \approx 1.14$ as in the experiments of McLemore for a blade twist of $\beta\left(\frac{r}{R} = 0.75\right) = 20°$. The resulting circulation distribution was specified for the *whole* range of the propeller rotational speed examined. This is of course a crude simplification. The experiments [10] were performed in the Langley full-scale windtunnel at $U_\infty = 94\,\mathrm{ft/s}$ corresponding to a hull REYNOLDS-number of $Re_L = 11.9 \cdot 10^6$. For this facility, a turbulence factor of $Tu \approx 0.003$ is reported. According to a correlation proposed by van Ingen [13] the effect of such a level of freestream turbulence on transition can be simulated by specifying a critical amplification factor of $n_{crit.} \approx 6.8$ for the $e^n$ criterion. This value of $n_{crit.}$ was used in the analysis of the viscous hull flow.

Fig. 15 shows the calculated propeller efficiency vs. the advance ratio in comparison to measured characteristics obtained for two different blade twist angles $\beta$. In the calculations the viscous interaction between hull and propeller and a fully-relaxing propeller slipstream was considered. Two curves are given, one as resulting for fully laminar and one for fully turbulent flow about the propeller blades. A direct comparison to the experiments is first of all admissible only for the advance ratio which serves to scale the bound circulation distribution ($\lambda = 1.14$). For this value of $\lambda$ the measured propeller efficiency lies right in between the predicted curves. But also for other rotational speeds the behaviour is determined quite reasonable even though a constant circulation distribution is assumed.

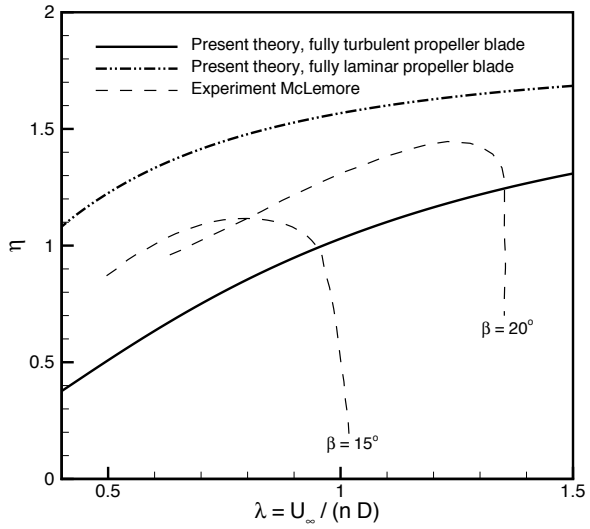


Figure 15: Calculated and measured efficiency of a stern propeller, experiment by McLemore [10], $Re_L(\text{hull}) = 11.9 \cdot 10^6$, natural transition ($n_{crit.}(\text{hull}) = 6.8$), $\alpha = 0°$

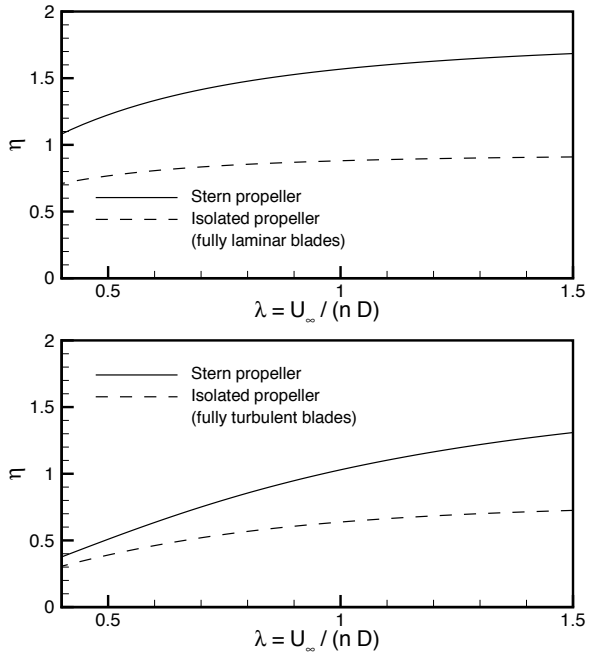


Figure 16: Calculated efficiency of a propeller located at the stern of the McLemore hull compared to an isolated propeller, upper picture: fully laminar blades, lower picture: fully turbulent blades

With decreasing $\lambda$ (increasing rotational speed at constant freestream velocity $U_\infty$) the viscous drag of the propeller blades becomes more dominant. This causes a reduction of the efficiency $\eta$. If the advance ratio is increased the effective angle of attack of the real propeller blades is decreased until the zero-lift incidence is reached and the propeller will not produce thrust anymore. A steep decrease of the efficiency can be observed in this $\lambda$-range. Because in the analysis the same finite circulation distribution is specified for every $\lambda$ regardless of the actual blade incidence this sharp drop does not result from the present calculation. The theoretical curves represent the result that would be achieved for a particular advance ratio if the twist distribution is adopted such that the intended circulation distribution is realized. As expected the efficiency increases continously with the advance ratio in this case.

Finally, in Fig. 16 the characteristics obtained for the stern propeller are compared to calculated efficiency curves which result for the isolated propeller in the absence of the hull. Identical circulation distributions are assumed in both cases. The results clearly show that the efficiency (based on $U_\infty$) is significantly increased if the propeller is located in the viscous wake of an upstream displacement body.

# 5 Summary

A tool for the calculation of the time-averaged flowfield about a displacement body with a stern-mounted propeller was developed. The method takes viscous interaction effects into account and enables, e.g., to determine the propeller-induced drag and to predict the characteristics of the wake propeller. The method was, at first, validated with respect to viscous flow calculation about the bare hull. It has shown that the coupled panel/boundary-layer procedure yields reasonable results even in the vicinity of the stern where a strong growth of the boundary layer can be observed.

Thereafter, the complete tool has been used to analyse different airship hulls propelled by a stern thruster. It has proven that the efficiency can be significantly increased if the propeller is located inside the viscous hull wake. Efficiencies well above 100% (based on $U_\infty$) found in experiments were also predicted by the present model. Taking the propeller-induced hull drag into account it was

demonstrated that the power required to propel the airship is decreasing for this favourable propeller installation. This, however, requires that the propeller is designed specifically for the real flow conditions in the propeller disc area since the blade incidence is significantly affected by the hull wake.

The present calculation method lacks from the fact that the bound circulation of the propeller blades is not determined during the analysis but has to be specified by the user. Furthermore, the detailed aerodynamic characteristics of the blade sections are not considered yet. Ongoing work deals with the extension of the model both respects.

## Acknowledgement

The present investigations were partly performed during a research stay of the first author at the Mechanical Engineering Laboratory, Tsukuba, Japan under grant of the Japan Industrial Technology Association. The authors gratefully acknowledge for this opportunity and for the support and the kind hospitality of the host Dr. M. Onda (MEL).

## References

[1] R. Eppler: *Airfoil Design and Data.* Springer Verlag Berlin Heidelberg New York, 1990. ISBN 3-540-52505-X.

[2] W.-H. Hucho: *Untersuchungen über den Einfluß einer Heckschraube auf die Druckverteilung und die Grenzschicht schiffsähnlicher Körper.* Dissertation, Technische Hochschule Braunschweig, Fakultät für Maschinenwesen, January 1967.

[3] J. C. LeBalleur: *Couplage visqueux non-visqueux: analyse du problème inculant décollements et ondes de choc.* La Récherche Aérospatiale, No. 6, 1977.

[4] R. C. Lock: *Prediction of the Drag of Wings at Subsonic Speeds by Viscous/Inviscid Interaction Techniques.* Aircraft Drag Prediction and Reduction, AGARD R-723, 1985.

[5] M. Lowag: *Druckverteilungsmessungen am Modell des Solarluftschiffs Lotte.* Studienarbeit, Institut für Aerodynamik und Gasdynamik, Universität Stuttgart, October 1999.

[6] Th. Lutz: *Berechnung und Optimierung subsonisch umströmter Profile und Rotationskörper.* Dissertation, Institut für Aerodynamik und Gasdynamik, Universität Stuttgart, 2000. VDI Fortschritt-Berichte, Reihe 7: Strömungstechnik, Nr. 378, ISBN 3-18-337807-8.

[7] Th. Lutz, D. Leinhos and S. Wagner: *Theoretical Investigations of the Flowfield of Airships with a Stern Propeller.* Proceedings of the International Airship Convention and Exhibition, 1996. Bedford, Great Britain, 5–7 July 1996.

[8] Th. Lutz and S. Wagner: *Drag Reduction and Shape Optimization of Airship Bodies.* Journal of Aircraft, Vol. 35, No. 3, S. 345–351, May–June 1998. AIAA Paper 97-1483.

[9] Th. Lutz and S. Wagner: *Numerical Shape Optimization of Natural Laminar Flow Bodies.* In: Proceedings of the 21st ICAS Congress, 13–18 September 1998, Melbourne, Australia, ICAS/AIAA, 1998. AIAA Paper 98-31525, ICAS-98-2.9.4.

[10] H. Clyde McLemore: *Wind Tunnel Tests of a 1/20-Scale Airship Model with Stern Propellers.* TN D-1026, NASA, 1962.

[11] V. C. Patel, A. Nakayama and R. Damian: *Measurements in the thick axisymmetric turbulent boundary layer near the tail of a body of revolution.* J. Fluid Mech., Vol. 63, No. 2, S. 345–367, 1974.

[12] T. W. Swafford: *Analytical Approximation of Two-Dimensional Separated Turbulent Boundary-Layer Velocity Profiles.* AIAA Journal, Vol. 21, No. 6, S. 923–925, 1983.

[13] J. L. van Ingen and L. M. M. Boermans: *Research on Laminar Separation Bubbles at Delft University of Technology in Relation to Low Reynolds Number Airfoil Aerodynamics.* Proceedings of the Conference on Low Reynolds Number Airfoil Aerodynamics, UNDAS-CP-77B123, University of Notre Dame, Indiana, USA, 1985, S. 89–124.